Strain-induced activation of symmetry-forbidden exciton-phonon couplings for enhanced phonon-assisted photoluminescence in MoS_2 monolayers

Rishabh Saraswat [1], Rekha Verma [1], and Sitangshu Bhattacharya [2]
[1] *Department of Electronics and Communication Engineering, Indian Institute of Information Technology-Allahabad, Uttar Pradesh 211015, India*
[2] *Electronic Structure Theory Group, Department of Electronics and Communication Engineering, Indian Institute of Information Technology-Allahabad, Uttar Pradesh 211015, India*

(Received 3 January 2025; revised 1 April 2025; accepted 6 May 2025; published 21 May 2025)

Phonon-assisted photoluminescence (PL) in molybdenum-based two-dimensional dichalcogenides is typically weak due to the dormant phonon coupling with optically inactive momentum-dark (intervalley) excitons, unlike in tungsten-based dichalcogenides where such processes are more prominent. Despite this inefficiency, we revisit excitons in MoS_2 using rigorous finite-momentum Bethe-Salpeter equation calculations to identify ways to enhance phonon-assisted recombination channels. Our *ab initio* results, complemented by group-theoretic analyses, reveal that while unstrained MoS_2 exhibits no phonon-assisted PL emissions at cryogenic temperatures due to forbidden A'' phonon modes, biaxial strain opens a pathway to significantly intensify this emission by activating hole-phonon A'-mediated scattering channels. By calculating allowed exciton-phonon matrix elements and scattering rates, we demonstrate how strain redistributes oscillator strengths toward radiative recombination. These findings provide a promising route to improve the PL emission efficiency in various metal dichalcogenide monolayers through strain engineering and offer valuable insights for further exploration of exciton-phonon dynamics, including time-resolved spectroscopic studies.

DOI: 10.1103/PhysRevB.111.205131

I. INTRODUCTION

Light emission in pristine semiconductors arises from the radiative recombination of bound electron-hole pairs, known as excitons. The nature of this emission—whether direct or indirect—is dictated by the excitonic dispersion, analogous to electronic band dispersion, particularly in relation to the valley center Γ in the excitonic Brillouin zone (BZ) [1]. Intravalley excitons form at the zero of the excitonic center-of-mass momentum ($\mathbf{Q} = 0$), which corresponds to the optical dipole limit. In this case, a direct optical gap occurs if the lowest-energy exciton is located at Γ, allowing efficient radiative recombination without additional momentum transfer, leading to intense direct photoluminescence (PL) [2]. In contrast, an indirect optical gap arises when the lowest exciton state lies at a finite momentum ($\mathbf{Q} \neq 0$), forming intervalley excitons, whose recombination necessitates phonon-mediated momentum transfer. While indirect processes are generally less efficient due to multiparticle interactions and selection rules, which suppress PL emission [3], bulk honeycomb (h)-boron nitride (BN) defies this limitation. Despite its indirect optical gap, exceptionally strong exciton-phonon coupling enables intense ultraviolet PL [4], with an efficiency surpassing even that of diamond [5].

Beyond bulk materials, high-quality two-dimensional (2D) transition-metal dichalcogenides (TMDs) provide an ideal platform to study spin-momentum-coupled exciton-light interactions. These noncentrosymmetric crystals, with time-reversal symmetry, feature two inequivalent valleys ($\mathbf{K}$ and $\mathbf{K}'$) in the electronic BZ, where spin-valley locking governs exciton formation [see Fig. 1(a)] [6,7]. Circularly polarized light with left or right handedness can selectively excite excitons in these valleys, leading to valley polarization [8–17]. The relative spin alignment of conduction and valence band edges at $\mathbf{K}$ and $\mathbf{K}'$ in W-based (WS_2, WSe_2) and Mo-based (MoS_2, $MoSe_2$) TMDs further imposes the selection criterion on exciton formation. Intravalley ($\mathbf{K}$-$\mathbf{K}$) excitons are bright if spin allowed (parallel spin) and dark if spin forbidden (antiparallel spin). In contrast, both spin-allowed and spin-forbidden intervalley ($\mathbf{K}$-$\mathbf{K}'$) excitons are momentum forbidden and thus optically dark [15,16,18–24]. Only bright intravalley excitons undergo radiative recombination, resulting in strong direct PL [16,18,21–24]. A key distinction exists between the ground-state excitons in W- and Mo-based TMDs. In W-based compounds, both intra- and intervalley ground-state excitons are degenerate and dark due to spin- and momentum-forbidden transitions [16,25], with dark-bright splittings of 40–50 meV [26]. In contrast, *ab initio* calculations predict that Mo-based TMDs host bright degenerate intra- and intervalley excitons [15], whereas experiments suggest a dark ground-state exciton with dark-bright splittings ranging from 14 to 100 meV [19,27].

Excitons that are dark, either by being spin or momentum forbidden, do not directly contribute to the PL, unless they are intentionally activated. This has been shown for the energetically lowest-lying dark intravalley spin-forbidden excitons. These excitons were observed to undergo a dark to bright transition in MoS_2 and $MoSe_2$ [27,28] by the spin-flipping process in an external in-plane magnetic field, or due to exchange interaction [29] or by phonon assistance such as in

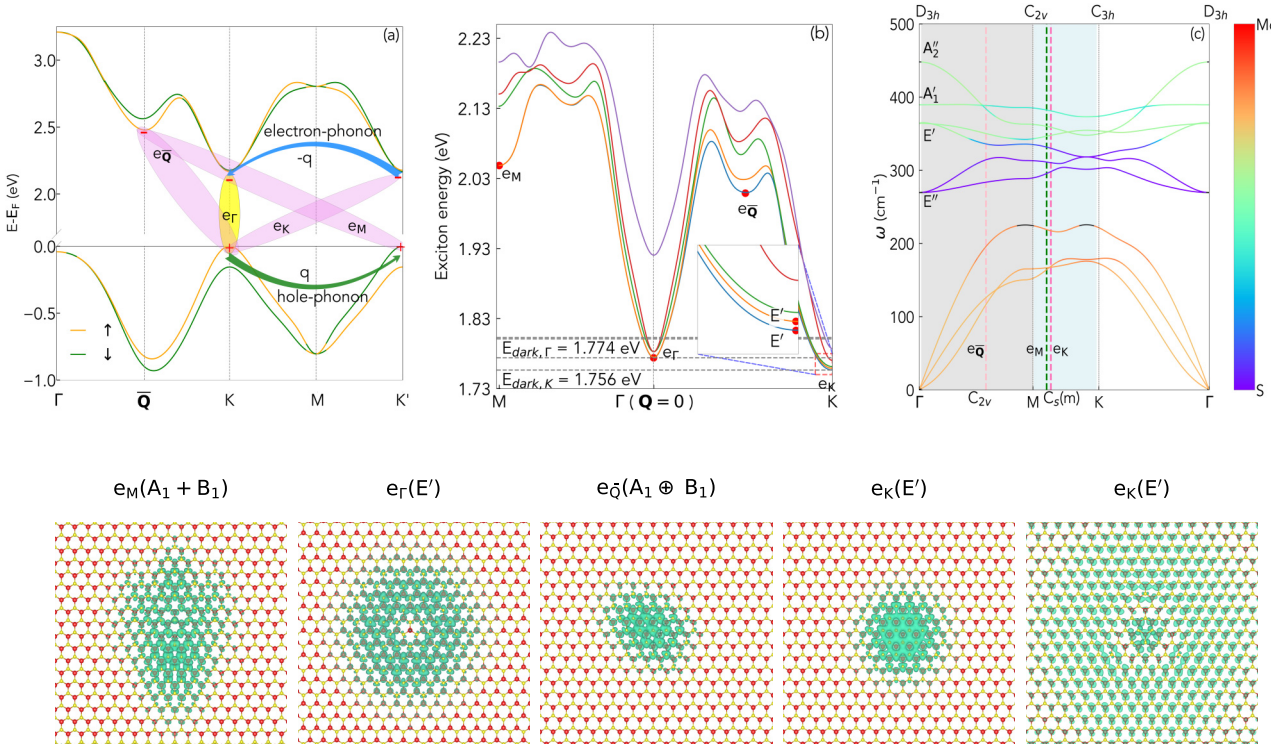

FIG. 1. Top panel: (a) Spin-resolved G_0W_0 corrected electron-energy dispersion in 1% biaxially tensile strained 2D h-MoS_2. The intravalley excitons (labeled as $e_{\mathbf{\Gamma}}$) are at $\mathbf{K}$ and $\mathbf{K}'$. The intervalley excitons ($e_{\mathbf{K}}$, $e_{\mathbf{M}}$, and $e_{\bar{\mathbf{Q}}}$) are, however, momentum forbidden. Only the top valence band is considered for holes, signifying the ground-state exciton. The electron-phonon and hole-phonon scattering processes responsible for PL emissions are shown by fancy arrows. (b) Corresponding excitonic energy dispersion showing the lowest five excitons along the BZ. The $\mathbf{\Gamma}$ point ($\mathbf{Q} = 0$) corresponds to $\mathbf{K}$ or $\mathbf{K}'$ in the electronic dispersion. The lowest five excitons at $\mathbf{\Gamma}$ in ascending order are 1 (labeled as $e_{\mathbf{\Gamma}}$), 2, 3, 4, and 5 (the degenerate partner of the fifth exciton, i.e., the sixth exciton, is not shown here). The inset magnifies the splitting of exciton energies at $\mathbf{K}$. (c) Phonon dispersion exhibiting phonon energy modes along the BZ. The individual atomic contribution is superimposed and shown by the color map. The dashed lines ($e_{\mathbf{K}}$ and $e_{\mathbf{M}}$) in the shaded area represent the two different phonon-assisted channels for exciton recombination in (a). Bottom panel (left to right): Excitonic probability distribution function and symmetry of the lowest exciton [shown by red circles in (b)] at momenta $\mathbf{M}$ ($e_{\mathbf{M}}$), $\mathbf{\Gamma}$ ($e_{\mathbf{\Gamma}}$), $\mathbf{Q}_{\mathbf{\Gamma}-\mathbf{K}}$ ($e_{\bar{\mathbf{Q}}}$), and $\mathbf{K}$ ($e_{\mathbf{K}}$).

WS_2 [30], leading to valley depolarization. The recombination of momentum forbidden dark excitons at cryogenic temperatures in $MoSe_2$ has been observed with varied outcomes. In one instance, no phonon-assisted PL is reported, though there is an asymmetry in the brightest direct PL signal toward higher energies [31]. In other observations, strong exciton-phonon (exc-ph) coupling appears, assisted by longitudinal acoustic (LA) phonons at the $\mathbf{M}$ point (in the phonon BZ) [32] and A_1' optical phonons at room temperature [33]. In contrast, WSe_2 consistently shows valley depolarization effects due to intense exc-ph scattering [31,34–39].

Although phonon-assisted PL emission has garnered significant attention in 2D h-$MoSe_2$, WS_2, and WSe_2, such a detailed mechanism in 2D h-MoS_2 remains largely unexplored. Therefore, in this work, we revisit 2D h-MoS_2 for a comprehensive understanding of phonon-assisted indirect excitonic recombination. While MoS_2 direct emission around room temperatures dominates at $\mathbf{\Gamma}$ in the excitonic BZ due to thermalization, we rather show using group-theoretic analyses that the cryogenic emission due to the low-energy dark excitons is forbidden by symmetry conditions. However, by harnessing strain engineering, these dark excitons can be activated to couple with the intervalley phonon mode (A') within the $\mathbf{M}$-$\mathbf{K}$ BZ route [see Fig. 1(c)], unlocking a pathway to enhanced indirect PL emission. We demonstrate these emissions using biaxial strain in the range of -0.5% to $+3\%$, achievable under standard laboratory conditions [40]. We illustrate that indirect PL emission at higher tensile strains in 2D MoS_2 is dominated by hole-phonon processes [see Fig. 1(a)], where the hole is scattered by a phonon from $\mathbf{K}$ to $\mathbf{K}'$, resulting in a recombination at $\mathbf{K}'$. The PL intensity peaks sharply at $+1\%$ strain, with a pronounced decline above and below this range due to a reduction in exc-ph coupling across different modes. These systematic findings can be useful as a textbook example to reveal the symmetry-driven indirect PL in 2D TMDs. The following discussions can also explain the nonmonotonic PL response to biaxial strain recently observed in 2D WSe_2 [41].

II. COMPUTATIONAL DETAILS

We employ fully relativistic, norm-conserving pseudopotentials [42] with core corrections for Mo (core: [Ca]; valence: $3d$, $4p$, $5s$, and $4d$) and S (core: [Ne]; valence: $3s$ and $3p$). Ground-state and excited-state computations were performed using the *ab initio* codes QUANTUM ESPRESSO [43] and YAMBO [44], respectively. A total of 200 electronic states (26

occupied, 174 unoccupied) was sufficient to converge quasiparticle (QP) gaps, with a screening matrix cutoff of 20 Ry for both QP energies and the Bethe-Salpeter (BS) equation. Convergence tests (see Supplemental Material (SM) [45]) indicate that an $18 \times 18 \times 1$ grid with Coulomb cutoff techniques [46] accurately reproduces excitonic energies within experimental ranges. Electron-phonon matrix elements (including self-energies [47] with Debye-Waller corrections [48]) and exc-ph matrix elements were computed on a converged $120 \times 120 \times 1$ transferred momenta fine grid. The implementation of *ab initio* biaxial strain and subsequent discussion on the electronic, phonon, and exciton energies including a comparison with reported experiments are summarized in Sec. I of the SM [45]. In the following discussion, we focus on results at +1% biaxial strain and compare them to other strain conditions as necessary.

III. RESULTS AND DISCUSSIONS

The indirect emission process is a two-step mechanism governed by Fermi's golden rule. An exciton transitions from its initial state $|\varphi_i\rangle$ to a final state $|\varphi_f\rangle$ via an intermediate state $|\varphi_t\rangle$. This involves a light coupling ($\hat{\varsigma}$) and phonon coupling ($\hat{g_{\mathbf{q}}}$), which may occur in either order. The entire process can then be described by $\langle\varphi_f|\hat{g}^{\dagger}_{\mathbf{q}}\hat{\varphi}|\varphi_i\rangle = \langle\varphi_f|\hat{g}^{\dagger}_{\mathbf{q}}|\varphi_t\rangle\langle\varphi_t|\hat{\varsigma}|\varphi_i\rangle$. The light-field polarization direction also imposes a condition on the coupling of phonon modes with excitons via the symmetry of states that are excited, aligning with the selection rules dictated by the crystal's point-group symmetry. Such cases are reported for bulk h-BN [49], where in-plane and out-of-plane light-field polarization selectively allows LA (longitudinal acoustic)/TA (transverse acoustic) and Z (out-of-plane) phonon modes coupling with excitons [50,51] and is found to be effective in overcoming limitations of indirect emission in WS_2 [52,53] and WSe_2 [54] by strain engineering.

For a 2D MoS_2, the D_{3h} point-group symmetry includes a fully symmetric (even) irreducible representation A'_1. The in-plane (two-dimensional) components, x and y, transform as the E' representation, enabling mixing and transitions allowed by symmetry. The out-of-plane z component transforms as A''_2, allowing additional transitions. Consequently, the overall transformation of the dipole operator can be expressed as $E'[x, y] + A''_2[z]$. This implies that when an incoming plane-polarized light field (commonly used in pump-probe experiments), represented by $E'[x, y]$, interacts with a ground state of symmetry A'_1, the resulting tensor product becomes $A'_1 \otimes E' = E'$. This corresponds to the symmetry of the energetically lowest doubly degenerate dark excitons ($e_{\mathbf{\Gamma}}$) at the $\mathbf{\Gamma}$ point.

To analyze the symmetry of the intervalley excitons, we performed a rigorous finite-momentum Bethe-Salpeter equation calculation for the lowest five excitonic energies and states across the entire Brillouin zone. Momentum conservation indicates that the intervalley exciton $e_{\mathbf{K}}$ in Fig. 1(a) corresponds to the exciton at the $\mathbf{K}$ point in the exciton dispersion shown in Fig. 1(b). Similarly, excitons $e_{\mathbf{M}}$ and $e_{\bar{\mathbf{Q}}}$ are located at the $\mathbf{M}$ and about $\frac{1}{2}|\mathbf{\Gamma} - \mathbf{K}|$ point, respectively. The degeneracy at $\mathbf{\Gamma}$ is lifted due to spin-orbit coupling along the $\mathbf{\Gamma}$-$\mathbf{K}$ direction. At the $\mathbf{K}$ point, the point-group symmetry reduces to C_{3h}. The two-dimensional irreducible representation E' transforms as the one-dimensional E' in C_{3h}, which is even with respect to the mirror symmetry σ_h and highlights that the charge densities are predominantly localized at the hole sites. This corresponds to the symmetry of the lowest two excitons $e_{\mathbf{K}}$ at $\mathbf{K}$. Similarly, the point-group symmetry at the $\mathbf{M}$ towards $\mathbf{\Gamma}$ reduces to C_{2v}, resulting in the double-point-group irreducible representation Γ_5, describing the degenerate excitons $e_{\mathbf{M}}$ at $\mathbf{M}$. Additionally, the exciton $e_{\bar{\mathbf{Q}}}$ falls within the C_{2v} group and as the degeneracy is lifted at this point, the split excitons have either $A_1 \oplus B_1$ symmetry. We emphasize that biaxial strain in the 2D system does not alter the crystalline point-group symmetry; thus, the symmetry representations remain invariant under applied strain. These symmetries are illustrated in the bottom panel of Fig. 1.

Similar to the electron-phonon matrix elements [55,56],

$$g_{mn,\nu}(\mathbf{k}, \mathbf{q}) = \langle m\mathbf{k}|\Delta V_{\nu\mathbf{q}}|n\mathbf{k} - \mathbf{q}\rangle, \tag{1}$$

where $g_{mn,\nu}(\mathbf{k}, \mathbf{q})$ denotes the electronic scattering probability amplitude for a transition from an initial Bloch state $|n\mathbf{k} - \mathbf{q}\rangle$ to a final state $|m\mathbf{k}\rangle$ via phonon absorption or emission and $\Delta V_{\nu\mathbf{q}}$ represents the Kohn-Sham potential perturbed by phonons, the exc-ph matrix elements in the excitonic basis can be written as [56–58]

$$\begin{aligned}\mathcal{G}_{\beta\lambda,\nu}(\mathbf{Q}, \mathbf{q}) &= \sum_{\upsilon,\upsilon',c,c',\mathbf{k}} A^{\upsilon,c,\mathbf{k}}_{\lambda,\mathbf{Q}}[g_{\upsilon\upsilon',\nu}(\mathbf{k} - \mathbf{Q}, \mathbf{q})\delta_{c,c'}]A^{\upsilon',c',\mathbf{k}^*}_{\beta,\mathbf{Q}+\mathbf{q}} \\ &\quad - \sum_{\upsilon,\upsilon',c,c',\mathbf{k}} A^{\upsilon,c,\mathbf{k}}_{\lambda,\mathbf{Q}}[g^*_{c'c,\nu}(\mathbf{k} + \mathbf{q}, \mathbf{q})\delta_{\upsilon,\upsilon'}]A^{\upsilon',c',\mathbf{k}+\mathbf{q}^*}_{\beta,\mathbf{Q}+\mathbf{q}},\end{aligned} \tag{2}$$

where $\mathcal{G}_{\beta\lambda,\nu}(\mathbf{Q}, \mathbf{q})$ now denotes the probability amplitude for scattering of an exciton λ into exciton β, mediated by absorption or emission of a phonon characterized by state $|\nu\mathbf{q}\rangle$. The coupling strength is defined as $|\mathcal{G}_{\beta\lambda,\nu}(\mathbf{Q}, \mathbf{q})|^2$. The exc-ph interaction in Eq. (2) can be interpreted as a quantum superposition of electron and hole scattering events with phonons, with each event weighted by the exciton wave function represented in the transition basis [59]. After incorporating the long- and short-range Coulomb Hartree potential (with reciprocal lattice vectors $\mathbf{G}$=0) in the finite-BS equation calculation and obtaining the phonon energies from density functional perturbation theory (DFPT), we computed the exc-ph coupling strength for the lowest exciton.

We highlight here the prominent phonon modes that strongly interact with the lowest indirect exciton. By analyzing the transferred momentum between the larger and reduced point-group symmetries [Fig. 1(c)], we identify intervalley modes between $\mathbf{M}$ and $\mathbf{K}$ with C_s(m) symmetry as key contributors. These modes belong to branches characterized by A' (even under σ_h) or A'' (odd under σ_h), which drive both indirect and direct scattering processes. Using the compatibility table [3], we find that the E' exciton at $\mathbf{K}$ reduces to A' in C_s(m), allowing symmetric coupling (see Table I). In contrast, when reducing to A'', the antisymmetric representation results in forbidden interactions. Consequently, modes 1, 4, 5, and 9, which are A'', do not contribute to indirect emission at any strain. This contrasts with excitons at $\mathbf{\Gamma}$, where all modes are symmetry allowed to couple. Figure 2 illustrates these interactions under various strain levels. The quantity

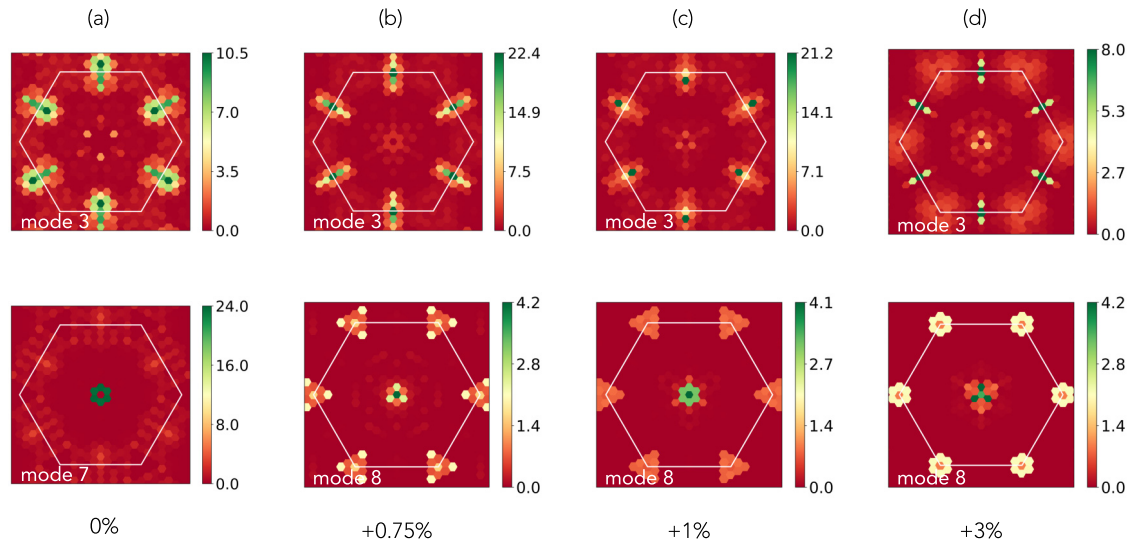

FIG. 2. (a)–(d) Phonon mode A' resolved gauge-invariant exc-ph coupling $|\mathcal{G}_{\beta\lambda,\nu}(\mathbf{Q},\mathbf{q})|^2$ across the exciton BZ at various strains. All values are normalized to 10^{-4} eV^2. Only the most prominent mode interaction contributing to the indirect and direct PL emission (see Fig. 6) is shown. The x and y axes are in transferred exciton momenta. The intensity of the color map shows the coupling strength.

shown represents the average coupling strength for transitions involving the low-energy excitonic states, specifically, $(\beta,\lambda) = (1,1), (1,2), (1,3), (1,4)$, and (1,5). This averaging procedure ensures that the presented coupling strength characterizes the phonon-mediated interactions primarily among these lowest-energy exciton states. For instance, Fig. 2(a) shows the unstrained case, where the only significant allowed modes are 3 and 7 that would exhibit a noticeable interaction with the lowest exciton between $\mathbf{\Gamma}$-$\mathbf{M}$ and around $\mathbf{\Gamma}$, respectively. While other modes are less significant, the subplot demonstrates that coupling between the $\mathbf{\Gamma}$ and $\mathbf{M}$ points is primarily driven by mode 3. However, mode 7 exhibits stronger coupling, predominantly interacting with excitons localized near $\mathbf{\Gamma}$. Figure 2(b) shows the exc-ph coupling strength at +0.75% strain for the lowest exciton interacting with phonon modes 3 and 8, with mode 3 having similar strength compared to the previous case.

At higher strain levels (+1% and +3%), as shown in Figs. 2(c) and 2(d), the coupling strength increases significantly compared to the respective modes (see Figs. S17–S23 in the SM [45] for plots of intermediate strain values). At +1%, modes 3 and 8 strongly interact with the lowest exciton near $\mathbf{M}$ and around $\mathbf{\Gamma}$, respectively. This observation aligns with the exciton dispersion in Fig. 1(b), which suggests phonon-assisted exciton scattering in these states. Additionally, mode 8 shows substantial interaction with the exciton near the $\mathbf{K}$ and $\mathbf{K}'$ points, indicating strong scattering in these regions. At +3%, the interaction distribution for mode 3 becomes more widespread across all high-symmetry points. However for mode 8, the interaction strength significantly drops out but becomes increasingly localized around the $\mathbf{\Gamma}$, $\mathbf{K}$, and $\mathbf{K}'$ points, reflecting a shift in the coupling dynamics.

In Fig. 3, we compute the scattering rate for the first five excitons at $\mathbf{Q} = 0$ (excitons 1 and 2 are degenerate dark, exciton 3 is bright, degenerate with the dark exciton 4, and exciton 5 is again dark) by evaluating the imaginary part of

TABLE I. Allowed exciton (lowest) and phonon-mode interactions in various point groups. Section II of the SM [45] contains a detailed discussion of our group-theoretic results.

Reduction to	Mode A' $[C_s(m)]$	Mode A'' $[C_s(m)]$
Exciton: E' at $\mathbf{K}$ (C_{3h})	A'	0
Exciton: Γ_5 at $\mathbf{M}$ (C_{2v})	$A' \oplus A''$	$A' \oplus A''$

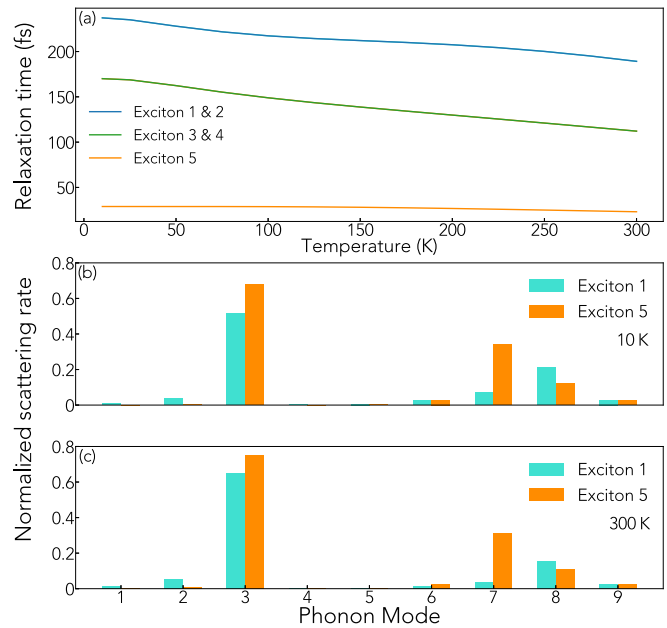

FIG. 3. (a) Relaxation time at +1% strain for the lowest five excitons: 1–5 [see Fig. 1(b)] at $\mathbf{Q} = 0$ (Γ) as a function of excitonic temperature (T_{exc}). Phonon-mode-resolved normalized scattering rates of excitons 1 and 5 at (b) 10 K and (c) 300 K.

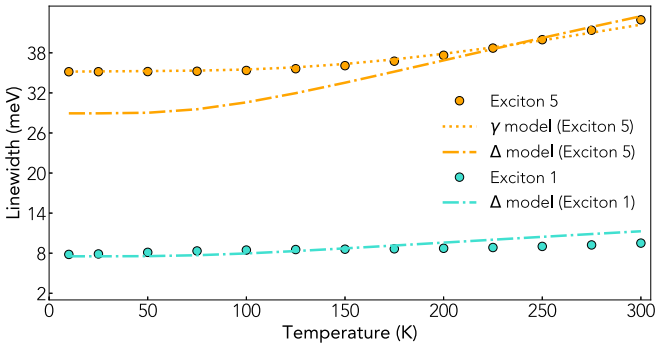

FIG. 4. Linewidth for exciton 1 and 5 at $\mathbf{\Gamma}$ as function of T_{exc} at +1% strain. Symbols are the *ab initio* result, whereas broken lines are fitted from the appropriate linewidth models.

the exc-ph coupling self-energy [56],

$$\Xi_\lambda(\mathbf{Q}=0;\omega) = \frac{1}{\Omega_{\text{BZ}}}\sum_{\mathbf{q},\nu\beta}\mathcal{G}_{\beta\lambda,\nu}(\mathbf{Q}=0,\mathbf{q})\mathcal{G}^*_{\beta\lambda,\nu}(\mathbf{Q}=0,\mathbf{q}) \times\left[\frac{1+n_{\mathbf{q},\nu}}{\omega-E_{\mathbf{q},\beta}+\omega_{\mathbf{q},\nu}+i\eta}+\frac{n_{\mathbf{q},\nu}}{\omega-E_{\mathbf{q},\beta}-\omega_{\mathbf{q},\nu}+i\eta}\right], \tag{3}$$

where Ω_{BZ} is the BZ volume and T_{exc} goes into the Boltzmann factor [50]. In Eq. (3), we neglect the temperature-dependent excitonic occupation factors, as they are negligibly small compared to phononic occupations. Additionally, we consider only the diagonal part of the self-energy. Under unstrained conditions, both our methodology and computed linewidth values align well with recent findings by Chan *et al.* [60]. To verify this, we directly compare our calculated linewidths with their results in Fig. 2(b) of the SM [45]. Our values closely match their linewidths, which are evaluated from the diagonal elements of the imaginary part of the exc-ph self-energy. Notable deviations appear only at higher temperatures, though these remain relatively small (of the order of a few meV).

The relaxation time is then given as the inverse of the scattering rate, which is plotted in Figs. 3(a)–3(c). From these plots, we see the general trend of increment of the scattering rate with temperature for all excitons [39], albeit with varying slopes. This indicates that higher temperatures lead to stronger exc-ph interactions across the spectrum. To gain further insight, we analyzed the contributions of individual phonon modes to the scattering rate at cryogenic (10 K) and room temperature (300 K) for the two excitons: exciton 1 and exciton 5 at $\mathbf{\Gamma}$. We note that the fifth exciton has a degenerate dark partner (sixth excitonic state), which is excluded from our calculations as convergence tests (see Fig. 30(b) in the SM [45]) show that five states suffice. The contributions are normalized to the total scattering rate at their respective temperatures. The impact of modes 3 and 8 on the scattering of the exciton 1 is evident and is attributed to the exc-ph interaction at both 10 and 300 K. In contrast, for the exciton 5, modes 3 and 7 are the primary contributors at these temperatures.

Figure 4 illustrates the linewidth (Δ) as a function of temperature for excitons 1 and 5 at $\mathbf{\Gamma}$. For exciton 1, the Δ is interpreted to fall under the strong-coupling regime following Toyozawa's equation [61,62],

$$\Delta = \sqrt{\Delta_{\text{A}}^2+\Delta_{\text{O}}^2}, \tag{4}$$

where $\Delta_{\text{A}}^2 = S_{\text{A}}E_{\text{A}}\coth(\frac{E_{\text{A}}}{2k_BT})$ represents the broadening due to acoustic phonons, and $\Delta_{\text{O}}^2 = S_{\text{O}}E_{\text{O}}[\exp(\frac{E_{\text{O}}}{2k_BT})-1]^{-1}$ accounts for the broadening caused by optical phonons. Here, S_{A} and S_{O} are the fitted exc-ph coupling strengths for acoustic and optical phonons, respectively, and E_{A} and E_{O} are their mean phonon energies. For exciton 1 under +1% strain, we fit the data using the parameters $S_{\text{A}} = 2.27$ meV, $S_{\text{O}} = 0.1$ meV, $E_{\text{A}} = 25$ meV, and $E_{\text{O}} = 48.1$ meV. In contrast, exciton 5 exhibits weak coupling at lower temperatures, which is modeled using

$$\gamma = \gamma_0 + aT + b\left[\exp\left(\frac{E_{\text{O}}}{k_BT}\right)-1\right]^{-1}, \tag{5}$$

where a (= 2 meV/K) and b (= 35 meV) represent the contributions from acoustic and optical phonon coupling, respectively, and γ_0 (= 35.1 meV) is a temperature-independent offset. For exciton 5, weak coupling dominates up to approximately 225 K. Beyond this temperature, the broadening transitions to being governed by strong coupling. However, it is noted that the linewidth roll-off rates remain relatively modest. We resolved that modes 3 and 8 for exciton 1, while 3 and 7 (A' for exciton 5), are responsible to account for such coupling in Δ.

To compute the PL intensity, we employ the van Roosbroeck-Shockley (RS) relation [56],

$$I^{\text{PL}}(\omega) = \text{Im}\sum_\lambda\frac{|T_\lambda|^2}{\pi^2\hbar c^3}\Bigg[\omega^3 n_r(\omega)\frac{1-R_\lambda}{\omega-E_\lambda+i\eta}e^{-\frac{E_\lambda-E_{\min}}{kT_{\text{exc}}}} + \sum_{\mu\beta\mathbf{q}}\omega(\omega\mp2\omega_{\mathbf{q}\mu})^2 n_r(\omega)|\mathcal{D}^{\pm}_{\beta\lambda,\mathbf{q}\mu}|^2 \times\frac{\frac{1}{2}\pm\frac{1}{2}+n_{\mathbf{q},\mu}}{\omega-(E_{\mathbf{q},\beta}\mp\omega_{\mathbf{q}\mu})+i\eta}e^{-\frac{E_{\mathbf{q},\beta}-E_{\min}}{kT_{\text{exc}}}}\Bigg], \tag{6}$$

where $|T_\lambda|^2$ are the excitonic dipoles, $n_r(\omega)$ is the refractive index, R_λ is the renormalization factor that measures the amount of spectral weight transferred to the satellites, E_λ are the excitonic energies, $E_{\min}$ is the minimum of the exciton dispersion, $|\mathcal{D}^{\pm}_{\beta\lambda,\mathbf{q}\nu}|^2$ are the phonon-assisted coupling strengths, and $E_{\mathbf{q},\beta}$ are the finite-momentum exciton energies. In our calculations, we incorporate a finite excitonic temperature which is used in all the temperature-dependent plots. We understand that this is an approximation for our case and the actual result will depend on the careful experiment between the bosonic and exciton temperatures, as shown in Cassabois *et al.* [4,56]. Unfortunately, we could not find such experimental data for MoS_2 to our best knowledge. Despite this, our PL and linewidth results for unstrained MoS_2 seem to be in strong agreement with experiments [see Fig. 2(b) in the SM and the inset in Fig. 5]. Additionally, a damping factor of 2 meV is applied to account for the exc-ph self-energy, and five virtual exciton states are included in the exc-ph scattering process.

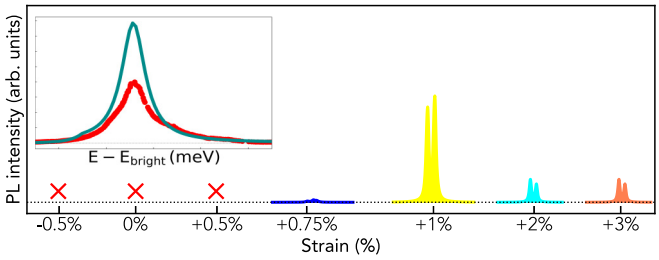

FIG. 5. Lowest-energy phonon replicas at 10 K for various strains. The × symbol denotes a forbidden indirect PL due to symmetry. The intensity scale is absolute. The inset shows the experimental cryogenic direct PL (symbols) from [27] for unstrained 2D MoS_2. The solid line is our *ab initio* result.

We note here that due to the presence of two distinct frequency components in the exciton-phonon Hamiltonian—originating from electron-electron and electron-phonon interactions—phonon-assisted PL cannot be directly obtained by solving this Hamiltonian. Instead, the PL spectrum is derived using the Green's function formalism, specifically through a first-order expansion of the finite-momentum exciton propagator with the dynamical exciton-phonon kernel in a Dyson-like equation. To achieve this, one should first compute the exciton propagator by solving the static finite-momentum BS equation in the absence of lattice vibrations. Next, using DFPT, the electron-phonon matrix elements are evaluated at the same **k** and **q** grids, ensuring mandatory convergence tests. These elements are then used to construct the exciton-phonon matrix elements and the corresponding self-energies within the framework of many-body perturbation theory [63], maintaining consistency in the transferred **Q** and **q** grids with additional convergence checks. The excitonic response is subsequently obtained by expanding the Dyson-like equation up to first order. Therefore, the electronic band renormalization induced by phonons does not enter the finite-momentum excitonic BS Hamiltonian. To ensure our analyses are on right track, we confirmed our excitonic dispersion to be in excellent agreement with Wu *et al.* [64] at the unstrained condition. Figure 5 illustrates the lowest-energy PL intensity peaks under various strain conditions. Our *ab initio* results for direct PL from an unstrained MoS_2 monolayer show excellent agreement with the experimental findings (inset in Fig. 5) [27]. We observe the emergence of a doublet structure, reaching its maximum at +1% strain driven by intense exc-ph interactions. This is in contrast to +0.75%, where the PL is only due to the dominant mode 8. To highlight this nonmonotonic behavior, we present the exciton thermalization process in Figs. 6(a)–6(d). Similar to Malic *et al.* [31], we demonstrate our PL emission energies with respect to the first bright exciton energy E_{bright} at **Γ** in the excitonic BZ. Consequently, all emissions to the left of the zero-energy line correspond to indirect processes. Our results can provide an insight to the recently reported PL emission by López *et al.* [41] for WSe_2. While López *et al.* attribute their similar nonmonotonic PL variation (see Fig. 3 in their work) to the energetic resonance of indirect excitons with defect-related states, we believe that contributions from intense symmetry-allowed exc-ph interactions, such as highlighted in this work, cannot be overlooked.

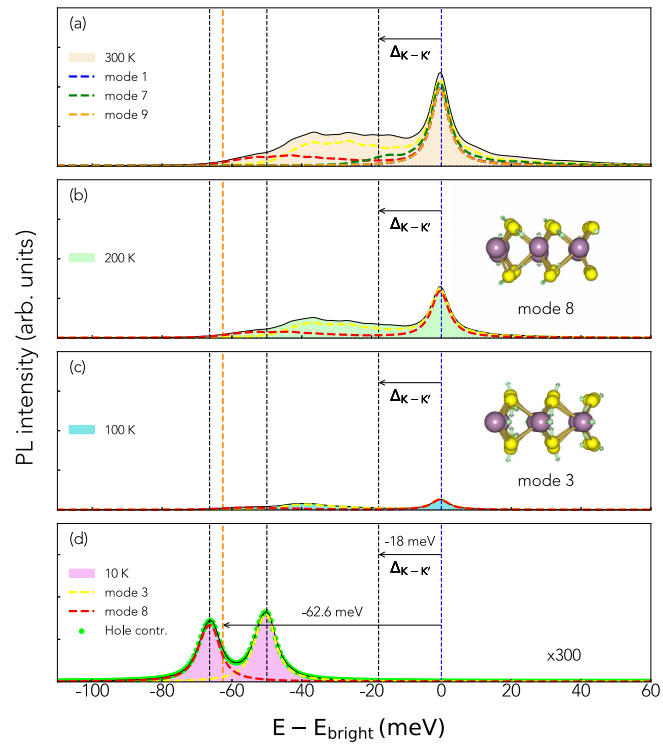

FIG. 6. (a)–(d) PL intensities with increasing T_{exc} at +1% strain demonstrating phonon replicas for modes 3 and 8. The energies are measured as a shift from the first bright exciton at Γ. The inset in (b) and (c) shows the atomic vibrations for modes 3 and 8. The dotted symbols in (d) represent the hole-phonon process in the PL intensity.

At cryogenic temperatures, as shown in Fig. 6(d), the emission lines exhibit two prominent phonon replicas. These Gaussian-type replicas, located approximately 50 and 70 meV below the bright line, are attributed to intervalley acoustic and optical modes 3 and 8, respectively, along the **M**-**K** direction [see the dashed line in Fig. 1(c) corresponding to the e_2 exciton]. Mode 3 originates from in-plane vibrations of Mo atoms (shear mode), while mode 8 corresponds to out-of-plane vibrations. The PL associated with the optical mode appears at lower energy than that of the acoustic mode. To discern whether the observed peaks arise from electron-phonon or hole-phonon scattering processes [see Eq. (6)], we evaluated the PL intensity separately for their contributions. Our analysis reveals that the lower-energy PL peak is primarily driven by hole-phonon scattering, where optical phonons facilitate hole scattering from **K** to **K′**, leading to recombination at **K′**. The strong exciton-phonon interaction responsible for this recombination is illustrated by the coupling matrix $|\mathcal{G}(\mathbf{Q},\mathbf{q})|^2$ in Fig. 2(c) and schematically depicted in Fig. 1(a). This behavior remains consistent at higher strains, exemplifying exciton scattering at **K** and **K′** as a transition from a no-phonon to a hole-phonon process.

The next higher-energy peak, around 50 meV, corresponds to excitons near **Γ** along the **Γ**-**M** direction, which involve small acoustic phonon energies for scattering. Excitons $e_{\mathbf{M}}$ and $e_{\bar{\mathbf{Q}}}$ scatter within themselves using intervalley optical phonon mode 8 (∼42 meV), but lack an available recombination path. Below 50 K, there is no significant exciton

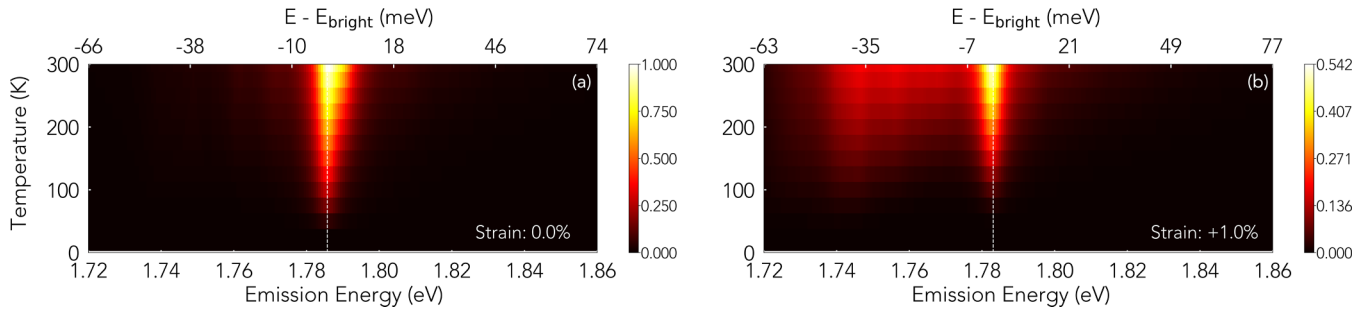

FIG. 7. Normalized PL intensities with varying temperatures at unstrained and +1% strain. The vertical dashed line in all cases shows the direct bright recombination.

thermalization that would result in a **Γ**-centered recombination channel. At 100 K, **Γ**-centered recombination begins to appear, predominantly driven by optical modes 7 and 9 (see Figs. 15–21 in the SM [45]). As the temperature increases, the lower-energy curves do not significantly shift, but broaden, with satellites emerging in the energy range 20–40 meV above and below the bright line. The emergence of the **Γ**-centered emission with increasing temperature, as shown in Figs. 6(a)–6(c), indicates the redistribution of oscillator strength between indirect and direct excitons. The dashed line, positioned 18 meV below the bright exciton, marks the energy of the lowest-lying momentum-indirect (**K**-**K**′) dark exciton. From this reference point, the threshold for longitudinal optical (LO) phonon-assisted emission is located approximately 44.6 meV away. Peaks appearing at energies lower (to the left) than this threshold arise predominantly from optical phonon-assisted transitions, as exemplified by the observed left peak corresponding to optical phonon mode 8. Conversely, peaks occurring at energies higher (to the right) are primarily attributed to acoustic phonon-assisted transitions, as illustrated by the right peak arising from acoustic phonon mode 3.

We now compare our results with that in tungsten-based TMDs reported by Malic *et al.* [31]. It is reported that the bright exciton resonances dominate the PL at higher temperatures (e.g., 150 and 300 K), leading to asymmetric emission spectra due to phonon-assisted recombination. In contrast, the recombination becomes more prominent at lower temperatures. Specifically, they found no observable phonon-assisted PL emission in unstrained Mo-based TMDs, consistent with our findings for unstrained MoS_2. However, under applied strain, our calculations in Fig. 6 reveal prominent phonon-assisted PL features at lower temperatures. At higher temperatures (200 and 300 K), the bright exciton resonance dominates again but exhibits asymmetry, consistent with observations in WSe_2 and WS_2. Notably, in strained MoS_2, phonon-assisted PL peaks appear approximately 50 and 70 meV below the bright exciton, aligning with reported shifts of 60 and 75 meV in WSe_2 and 70 and 90 meV in WS_2, respectively. Malic *et al.* also noted a splitting of the phonon-assisted peak in hBN-encapsulated WSe_2 samples [65–69], revealing two distinct phonon-assisted emission features. A similar trend is observed in our calculations on strained MoS_2, predicting two peaks from different phonon modes: the peak closer to the bright exciton originates from the third phonon mode, while the more distant peak stems from the eighth mode.

To understand the shift in emission energy and the evolution of PL intensity with temperature, we present results under unstrained and +1% strain conditions in Figs. 7(a) and 7(b). A clear redshift of the bright emission is observed with increasing strain. Under unstrained conditions, faint indirect emission is visible near 1.73 eV, while the direct bright emission remains the strongest among all strain conditions. At lower strains (see Fig. S25 in the SM [45]), the direct path intensities become most prominent due to satellite weights that thermalize at higher temperatures. The maximum intensity of the indirect excitons at cryogenic temperatures is observed at +1% strain. At higher strain levels, the indirect emissions become more distributed, but their intensities drop due to weaker exciton-phonon couplings. The appearance of doublet peaks at higher strains (beyond +1%) reverses their intensity magnitude, as shown in Fig. 5, due to the additive contribution from other low-energy modes. Additional work remains to identify the symmetries of the indirect spin-split excitons $e_{\mathbf{K}}$ with respect to C_3 rotation, which will be addressed in future studies.

We now discuss the limitation of our work. The formalism of exc-ph coupling in Eq. (2) must be invariant if an arbitrary phase is added to the electronic wave functions entering the electron-phonon coupling [Eq. (1)] and the exciton coefficients (A terms) in Eq. (2). To preserve this gauge invariance, the same Kohn-Sham electronic wave function set $|n\mathbf{k}\rangle$ should be used, which is defined up to an arbitrary phase fixed by the specific simulation, for both the DFPT and BS steps. Otherwise, joining the g elements with the A coefficient as complex numbers, like in Eq. (2), will lead to numerical noise and unphysical effects. This is a typical phase mismatch which generates error both in the intensity peak magnitude as well as exciton lifetime. To the best of our knowledge, with the recent codes of QUANTUM ESPRESSO and YAMBO, this is impossible to do. For comparison, we highlight the works of Zanfrognini *et al.* [49] and Bernardi *et al.* [59], where the PERTURBO code [70], when combined with YAMBO, successfully reproduces the correct intensity levels corresponding to experimental peaks for bulk h-BN. Due to the complexity of interfacing these codes, our procedure does not utilize the YAMBO-PERTURBO interface. Thus, in this case, there could be a phase mismatch which can show an opposite trend in the intensity levels, similar to Lechifflart *et al.* [56]. We have compared our exciton-phonon coupling results for the lowest-lying dark exciton with those of Chan *et al.* [60] (see Fig. 2(b) in the SM [45]). We find that apart from the alternating pat-

terns around the **M** point and the anomalous emergence of high coupling strength near the Γ point in our Fig. 2 (which we attribute to phase mismatch), our results are in strong agreement. A similar observation holds for the lowest-lying bright exciton (*A* exciton).

IV. CONCLUSIONS

In summary, we investigate *ab initio* exciton-phonon couplings in 2D MoS_2 using a quantum superposition approach for electron and hole scattering events with phonons. Through rigorous *ab initio* calculations and group-theoretic analyses, we demonstrate that indirect emission in 2D MoS_2 under in-plane light polarization is symmetry allowed for both acoustic and optical phonon modes with A' character. This systematic study serves as a textbook example of how indirect exciton recombination, absent in the compressive and unstrained cases, becomes dominated by hole-phonon scattering processes (**K** to **K**′ transitions) under tensile strain. We find that this transition maximizes the indirect emission around +1% strain at cryogenic temperatures, driven by enhanced exciton-phonon scatterings assisted by intervalley A' phonon modes with reduced point group C_s(m). These results provide an alternative explanation for the nonmonotonic PL variations with strain reported in recent experiments [41].

ACKNOWLEDGMENTS

This work was carried out with financial support from SERB, India with Grant No. CRG/2023/000476. We thank the National Super Computing Mission (NSM) "Paramshivay" at IIT BHU, India for providing computing resources.

DATA AVAILABILITY

The data that support the findings of this article are openly available [123]; embargo periods may apply.

[1] R. S. Knox, *Theory of Excitons* (Academic Press, New York, London, 1963), p. 100.
[2] P. T. Landsberg, *Recombination in Semiconductors* (Cambridge University Press, Cambridge, 1992).
[3] M. S. Dresselhaus, G. Dresselhaus, and A. Jorio, *Group Theory: Application to the Physics of Condensed Matter*, 1st ed. (Springer-Verlag, Berlin, Germany, 2008).
[4] G. Cassabois, P. Valvin, and B. Gil, Hexagonal boron nitride is an indirect band gap semiconductor, Nat. Photon. **10**, 262 (2016).
[5] L. Schué, L. Sponza, A. Plaud, H. Bensalah, K. Watanabe, T. Taniguchi, F. Ducastelle, A. Loiseau, and J. Barjon, Bright luminescence from indirect and strongly bound excitons in h-BN, Phys. Rev. Lett. **122**, 067401 (2019).
[6] W. Yao, D. Xiao, and Q. Niu, Coupled spin and valley physics in monolayers of MoS_2 and other group-VI dichalcogenides, Phys. Rev. B **77**, 235406 (2008).
[7] D. Xiao, G.-B. Liu, W. Feng, X. Xu, and W. Yao, Valley-dependent optoelectronics from inversion symmetry breaking, Phys. Rev. Lett. **108**, 196802 (2012).
[8] T. Cao, G. Wang, W. Han, H. Ye, C. Zhu, J. Shi, Q. Niu, P. Tan, E. Wang, B. Liu, and J. Feng, Valley-selective circular dichroism of monolayer molybdenum disulphide, Nat. Commun. **3**, 887 (2012).
[9] H. Zeng, J. Dai, W. Yao, D. Xiao, and X. Cui, Valley polarization in MoS_2 monolayers by optical pumping, Nat. Nanotechnol. **7**, 490 (2012).
[10] K. F. Mak, K. He, J. Shan, and T. F. Heinz, Control of valley polarization in monolayer MoS_2 by optical helicity, Nat. Nanotechnol. **7**, 494 (2012).
[11] A. M. Jones, H. Yu, N. J. Ghimire, S. Wu, G. Aivazian, J. S. Ross, B. Zhao, J. Yan, D. G. Mandrus, D. Xiao, W. Yao, and X. Xu, Optical generation of excitonic valley coherence in monolayer WSe_2, Nat. Nanotechnol. **8**, 634 (2013).
[12] A. Srivastava, M. Sidler, A. V. Allain, D. S. Lembke, A. Kis, and A. Imamoglu, Valley Zeeman effect in elementary optical excitations of monolayer WSe_2, Nat. Phys. **11**, 141 (2015).
[13] J. P. Echeverry, B. Urbaszek, T. Amand, X. Marie, and I. C. Gerber, Splitting between bright and dark excitons in transition metal dichalcogenide monolayers, Phys. Rev. B **93**, 121107(R) (2016).
[14] T. Deilmann and K. S. Thygesen, Dark excitations in monolayer transition metal dichalcogenides, Phys. Rev. B **96**, 201113(R) (2017).
[15] E. Malic, M. Selig, M. Feierabend, S. Brem, D. Christiansen, F. Wendler, A. Knorr, and G. Berghuser, Dark excitons in transition metal dichalcogenides, Phys. Rev. Mater. **2**, 014002 (2018).
[16] G. Wang, A. Chernikov, M. M. Glazov, T. F. Heinz, X. Marie, T. Amand, and B. Urbaszek, *Colloquium*: Excitons in atomically thin transition metal dichalcogenides, Rev. Mod. Phys. **90**, 021001 (2018).
[17] T. Mueller and E. Malic, Exciton physics and device application of two-dimensional transition metal dichalcogenide semiconductors, npj 2D Mater. Appl. **2**, 29 (2018).
[18] A. Splendiani, L. Sun, Y. Zhang, T. Li, J. Kim, C.-Y. Chim, G. Galli, and F. Wang, Emerging photoluminescence in monolayer MoS_2, Nano Lett. **10**, 1271 (2010).
[19] M. R. Molas, C. Faugeras, A. O. Slobodeniuk, K. Nogajewski, M. Bartos, D. M. Basko, and M. Potemski, Brightening of dark excitons in monolayers of semiconducting transition metal dichalcogenides, 2D Mater. **4**, 021003 (2017).
[20] C. Robert, R. Picard, D. Lagarde, G. Wang, J. P. Echeverry, F. Cadiz, P. Renucci, A. Högele, T. Amand, X. Marie *et al.*, Excitonic properties of semiconducting monolayer and bilayer $MoTe_2$, Phys. Rev. B **94**, 155425 (2016).
[21] H. R. Gutiérrez, N. Perea-López, A. L. Elías, A. Berkdemir, B. Wang, R. Lv, F. López-Urías, V. H. Crespi, H. Terrones, and M. Terrones, Extraordinary room-temperature photoluminescence in triangular WS_2 monolayers, Nano Lett. **13**, 3447 (2013).
[22] Y. Zhang, T.-R. Chang, B. Zhou, Y.-T. Cui, H. Yan, Z. Liu, F. Schmitt, J. Lee, R. Moore, Y. C. *et al.*, Direct observation of the transition from indirect to direct band gap in atomically thin epitaxial $MoSe_2$, Nat. Nanotechnol. **9**, 111 (2014).

[23] M. Palummo, M. Bernardi, and J. C. Grossman, Exciton radiative lifetimes in two-dimensional transition metal dichalcogenides, Nano Lett. **15**, 2794 (2015).

[24] K. He, N. Kumar, L. Zhao, Z. Wang, K. F. Mak, H. Zhao, and J. Shan, Tightly bound excitons in monolayer WSe_2, Phys. Rev. Lett. **113**, 026803 (2014).

[25] X.-X. Zhang, Y. You, S. Y. F. Zhao, and T. F. Heinz, Experimental evidence for dark excitons in monolayer WSe_2, Phys. Rev. Lett. **115**, 257403 (2015).

[26] Y. Zhou, G. Scuri, D. S. Wild, A. A. High, A. Dibos, L. A. Jauregui, C. Shu, K. D. Greve, K. Pistunova, A. Y. Joe, T. Taniguchi, K. Watanabe, P. Kim, M. D. Lukin, and H. Park, Probing dark excitons in atomically thin semiconductors via near-field coupling to surface plasmon polaritons, Nat. Nanotechnol. **12**, 856 (2017).

[27] C. Robert, B. Han, P. Kapuscinski, A. Delhomme, C. Faugeras, T. Amand, M. R. Molas, M. Bartos, K. Watanabe, T. Taniguchi, B. Urbaszek, M. Potemski, and X. Marie, Measurement of the spin-forbidden dark excitons in MoS_2 and $MoSe_2$ monolayers, Nat. Commun. **11**, 4037 (2020).

[28] X.-X. Zhang, T. Cao, Z. Lu, Y.-C. Lin, F. Zhang, Y. Wang, Z. Li, J. C. Hone, J. A. Robinson, D. Smirnov, S. G. Louie, and T. F. Heinz, Magnetic brightening and control of dark excitons in monolayer WSe_2, Nat. Nanotechnol. **12**, 883 (2017).

[29] T. Yu and M. W. Wu, Valley depolarization due to intervalley and intravalley electron-hole exchange interactions in monolayer MoS_2, Phys. Rev. B **89**, 205303 (2014).

[30] Z. Wang, A. Molina-Sánchez, P. Altmann, D. Sangalli, D. D. Fazio, G. Soavi, U. Sassi, F. Bottegoni, F. Ciccacci, M. Finazzi, L. Wirtz, A. C. Ferrari, A. Marini, G. Cerullo, and S. D. Conte, Intravalley spin–flip relaxation dynamics in single-layer WS_2, Nano Lett. **18**, 6882 (2018).

[31] S. Brem, A. Ekman, D. Christiansen, F. Katsch, M. Selig, C. Robert, X. Marie, B. Urbaszek, A. Knorr, and E. Malic, Phonon-assisted photoluminescence from indirect excitons in monolayers of transition-metal dichalcogenides, Nano Lett. **20**, 2849 (2020).

[32] C. M. Chow, H. Yu, A. M. Jones, J. R. Schaibley, M. Koehler, D. G. Mandrus, R. Merlin, W. Yao, and X. Xu, Phonon-assisted oscillatory exciton dynamics in monolayer $MoSe_2$, npj 2D Mater. Appl. **1**, 33 (2017).

[33] D. Li, C. Trovatello, S. D. Conte, M. Nuß, G. Soavi, G. Wang, A. C. Ferrari, G. Cerullo, and T. Brixner, Exciton-phonon coupling strength in single-layer $MoSe_2$ at room temperature, Nat. Commun. **12**, 954 (2021).

[34] S. Zheng, J.-K. So, F. Liu, Z. Liu, N. Zheludev, and H. J. Fan, Giant enhancement of cathodoluminescence of monolayer transitional metal dichalcogenides semiconductors, Nano Lett. **17**, 6475 (2017).

[35] V. Chellappan, A. L. C. Pang, S. Sarkar, Z. E. Ooi, and K. E. J. Goh, Effect of phonons on valley depolarization in monolayer WSe_2, Electron. Mater. Lett. **14**, 766 (2018).

[36] Y. Miyauchi, S. Konabe, F. Wang, W. Zhang, A. Hwang, Y. Hasegawa, L. Zhou, S. Mouri, M. Toh, G. Eda, and K. Matsuda, Evidence for line width and carrier screening effects on excitonic valley relaxation in 2D semiconductors, Nat. Commun. **9**, 2598 (2018).

[37] T.-Y. Jeong, S. Bae, S.-Y. Lee, S. Jung, Y.-H. Kim, and K.-J. Yee, Valley depolarization in monolayer transition-metal dichalcogenides with zone-corner acoustic phonons, Nanoscale **12**, 22487 (2020).

[38] V. Funk, K. Wagner, E. Wietek, J. D. Ziegler, J. Forste, J. Lindlau, M. Forg, K. Watanabe, T. Taniguchi, A. Chernikov, and A. Hogele, Spectral asymmetry of phonon sideband luminescence in monolayer and bilayer WSe_2, Phys. Rev. Res. **3**, L042019 (2021).

[39] H.-Y. Chen, D. Sangalli, and M. Bernardi, First-principles ultrafast exciton dynamics and time-domain spectroscopies: Dark-exciton mediated valley depolarization in monolayer WSe_2, Phys. Rev. Res. **4**, 043203 (2022).

[40] H. Li, A. W. Contryman, X. Qian, S. M. Ardakani, Y. Gong, X. Wang, J. M. Weisse, C. H. Lee, J. Zhao, P. M. Ajayan, J. Li, H. C. Manoharan, and X. Zheng, Optoelectronic crystal of artificial atoms in strain-textured molybdenum disulphide, Nat. Commun. **6**, 7381 (2015).

[41] P. H. López, S. Heeg, C. Schattauer, S. Kovalchuk, A. Kumar, D. J. Bock, J. N. Kirchhof, B. Höfer, K. Greben, D. Yagodkin, L. Linhart, F. Libisch, and K. I. Bolotin, Strain control of hybridization between dark and localized excitons in a 2D semiconductor, Nat. Commun. **13**, 7691 (2022).

[42] D. R. Hamann, Optimized norm-conserving Vanderbilt pseudopotentials, Phys. Rev. B **88**, 085117 (2013).

[43] P. Giannozzi, O. Andreussi, T. Brumme, O. Bunau, M. B. Nardelli, M. Calandra, R. Car, C. Cavazzoni, D. Ceresoli, M. C. *et al.*, Advanced capabilities for materials modelling with QUANTUM ESPRESSO, J. Phys.: Condens. Matter **29**, 465901 (2017).

[44] D. Sangalli, A. Ferretti, H. Miranda, C. Attaccalite, I. Marri, E. Cannuccia, P. Melo, M. Marsili, F. Paleari, A. Marrazzo *et al.*, Many-body perturbation theory calculations using the YAMBO code, J. Phys.: Condens. Matter **31**, 325902 (2019).

[45] See Supplemental Material at http://link.aps.org/supplemental/10.1103/PhysRevB.111.205131 for necessary convergence, supporting figures, theoretical and reported experimental discussions, which also includes Refs. [71–122].

[46] A. Guandalini, P. D'Amico, A. Ferretti, and D. Varsano, Efficient GW calculations in two dimensional materials through a stochastic integration of the screened potential, npj Comput. Mater. **9**, 44 (2023).

[47] H. Y. Fan, Temperature dependence of the energy gap in monatomic semiconductors, Phys. Rev. **78**, 808 (1950).

[48] E. Cannuccia and A. Marini, Effect of the quantum zero-point atomic motion on the optical and electronic properties of diamond and trans-polyacetylene, Phys. Rev. Lett. **107**, 255501 (2011).

[49] M. Zanfrognini, A. Plaud, I. Stenger, F. Fossard, L. Sponza, L. Schué, F. Paleari, E. Molinari, D. Varsano, L. Wirtz, F. Ducastelle, A. Loiseau, and J. Barjon, Distinguishing different stackings in layered materials via luminescence spectroscopy, Phys. Rev. Lett. **131**, 206902 (2023).

[50] F. Paleari, H. P. C. Miranda, A. Molina-Sanchez, and L. Wirtz, Exciton-phonon coupling in the ultraviolet absorption and emission spectra of bulk hexagonal boron nitride, Phys. Rev. Lett. **122**, 187401 (2019).

[51] T. Q. P. Vuong, G. Cassabois, P. Valvin, V. Jacques, A. V. D. Lee, A. Zobelli, K. Watanabe, T. Taniguchi, and B. Gil, Phonon symmetries in h-BN probed by incoherent light emission, 2D Mater. **4**, 011004 (2016).

[52] Y. Pan and F. Caruso, Strain-induced activation of chiral-phonon emission in monolayer WS_2, npj 2D Mater. Appl. **8**, 42 (2024).

[53] T. Chowdhury, S. Chatterjee, D. Das, I. Timokhin, P. D. Nunez, M. A. Gokul, S. Chatterjee, K. Majumdar, P. Ghosh, A. Mishchenko, and A. Rahman, Strain-induced activation of chiral-phonon emission in monolayer WS_2, Phys. Rev. B **110**, L081405 (2024).

[54] B. Aslan, M. Deng, and T. F. Heinz, Strain tuning of excitons in monolayer WSe_2, Phys. Rev. B **98**, 115308 (2018).

[55] F. Giustino, Electron-phonon interactions from first principles, Rev. Mod. Phys. **89**, 015003 (2017).

[56] P. Lechifflart, F. Paleari, D. Sangalli, and C. Attaccalite, First-principles study of luminescence in hexagonal boron nitride single layer: Exciton-phonon coupling and the role of substrate, Phys. Rev. Mater. **7**, 024006 (2023).

[57] G. Marini, M. Calandra, and P. Cudazzo, Optical absorption and photoluminescence of single-layer boron nitride from a first-principles cumulant approach, Nano Lett. **24**, 6017 (2024).

[58] F. Paleari, First-principles approaches to the description of indirect absorption and luminescence spectroscopy: Exciton-phonon coupling in hexagonal boron nitride, Ph.D. thesis, Université du Luxembourg, 2019.

[59] H.-Y. Chen, D. Sangalli, and M. Bernardi, Exciton-phonon interaction and relaxation times from first principles, Phys. Rev. Lett. **125**, 107401 (2020).

[60] Y.-h. Chan, J. B. Haber, M. H. Naik, J. B. Neaton, D. Y. Qiu, F. H. da Jornada, and S. G. Louie, Exciton lifetime and optical line width profile via exciton-phonon interactions: Theory and first-principles calculations for monolayer MoS_2, Nano Lett. **23**, 3971 (2023).

[61] Y. Toyozawa, Theory of line-shapes of the exciton absorption bands, Prog. Theor. Phys. **20**, 53 (1958).

[62] T. Q. P. Vuong, G. Cassabois, P. Valvin, S. Liu, J. H. Edgar, and B. Gil, Exciton-phonon interaction in the strong-coupling regime in hexagonal boron nitride, Phys. Rev. B **95**, 201202(R) (2017).

[63] G. D. Mahan, *Many-Particle Physics*, 3rd ed. (Springer International, New York, 2014).

[64] F. Wu, F. Qu, and A. H. MacDonald, Exciton band structure of monolayer MoS_2, Phys. Rev. B **91**, 075310 (2015).

[65] Z. Ye, L. Waldecker, E. Y. Ma, D. Rhodes, A. Antony, B. Kim, X.-X. Zhang, M. Deng, Y. Jiang, Z. Lu, D. Smirnov, K. Watanabe, T. Taniguchi, J. Hone, and T. F. Heinz, Efficient generation of neutral and charged biexcitons in encapsulated WSe_2 monolayers, Nat. Commun. **9**, 3718 (2018).

[66] Z. Li, T. Wang, C. Jin, Z. Lu, Z. Lian, Y. Meng, M. Blei, S. Gao, T. Taniguchi, K. Watanabe, T. Ren, S. Tongay, L. Yang, D. Smirnov, T. Cao, and S.-F. Shi, Emerging photoluminescence from the dark-exciton phonon replica in monolayer WSe_2, Nat. Commun. **10**, 2469 (2019).

[67] E. Courtade, M. Semina, M. Manca, M. M. Glazov, C. Robert, F. Cadiz, G. Wang, T. Taniguchi, K. Watanabe, M. Pierre, W. Escoffier, E. L. Ivchenko, P. Renucci, X. Marie, T. Amand, and B. Urbaszek, Charged excitons in monolayer WSe_2: Experiment and theory, Phys. Rev. B **96**, 085302 (2017).

[68] J. Lindlau, C. Robert, V. Funk, J. Forste, M. Forg, L. Colombier, A. Neumann, E. Courtade, S. Shree, T. Taniguchi, K. Watanabe, M. M. Glazov, X. Marie, B. Urbaszek, and A. Hogele, Identifying optical signatures of momentum-dark excitons in transition metal dichalcogenide monolayers, arXiv:1710.00988v2.

[69] M. Barbone, A. R.-P. Montblanch, D. M. Kara, C. Palacios-Berraquero, A. R. Cadore, D. De Fazio, B. Pingault, E. Mostaani, H. Li, B. Chen, K. Watanabe, T. Taniguchi, S. Tongay, G. Wang, A. C. Ferrari, and M. Atatüre, Charge-tuneable biexciton complexes in monolayer WSe_2, Nat. Commun. **9**, 3721 (2018).

[70] J.-J. Zhou, J. Park, I.-T. Lu, I. Maliyov, X. Tong, and M. Bernardi, Perturbo: A software package for *ab initio* electron-phonon interactions, charge transport and ultrafast dynamics, Comput. Phys. Commun. **264**, 107970 (2021).

[71] G. Strinati, Dynamical shift and broadening of core excitons in semiconductors, Phys. Rev. Lett. **49**, 1519 (1982).

[72] G. Onida, L. Reining, and A. Rubio, Electronic excitations: Density-functional versus many-body Green's-function approaches, Rev. Mod. Phys. **74**, 601 (2002).

[73] M. Rohlfing and S. G. Louie, Electron-hole excitations and optical spectra from first principles, Phys. Rev. B **62**, 4927 (2000).

[74] R. W. Godby and R. J. Needs, Metal-insulator transition in Kohn-Sham theory and quasiparticle theory, Phys. Rev. Lett. **62**, 1169 (1989).

[75] O. Pulci, G. Onida, R. Del Sole, and L. Reining, *Ab initio* calculation of self-energy effects on optical properties of GaAs(110), Phys. Rev. Lett. **81**, 5374 (1998).

[76] C. A. Rozzi, D. Varsano, A. Marini, E. K. U. Gross, and A. Rubio, Exact Coulomb cutoff technique for supercell calculations, Phys. Rev. B **73**, 205119 (2006).

[77] N. Kumar, M. Kolos, S. Bhattacharya, and F. Karlický, Excitons, optical spectra, and electronic properties of semiconducting Hf-based mxenes, J. Chem. Phys. **160**, 124707 (2024).

[78] D. Kammerlander, S. Botti, M. A. L. Marques, A. Marini, and C. Attaccalite, Speeding up the solution of the Bethe-Salpeter equation by a double-grid method and Wannier interpolation, Phys. Rev. B **86**, 125203 (2012).

[79] A. F. Rigosi, H. M. Hill, K. T. Rim, G. W. Flynn, and T. F. Heinz, Electronic band gaps and exciton binding energies in monolayer Mo_x W_{1-x} S_2 transition metal dichalcogenide alloys probed by scanning tunneling and optical spectroscopy, Phys. Rev. B **94**, 075440 (2016).

[80] S. Park, N. Mutz, T. Schultz, S. Blumstengel, A. Han, A. Aljarb, L.-J. Li, E. J. W. List-Kratochvil, P. Amsalem, and N. Koch, Direct determination of monolayer MoS_2 and WSe_2 exciton binding energies on insulating and metallic substrate, 2D Mater. **5**, 025003 (2018).

[81] H. M. Hill, A. F. Rigosi, C. Roquelet, A. Chernikov, T. C. Berkelbach, D. R. Reichman, M. S. Hybertsen, L. E. Brus, and T. F. Heinz, Observation of excitonic Rydberg states in monolayer $MoS_2$and WS_2 by photoluminescence excitation spectroscopy, Nano Lett. **15**, 2992 (2015).

[82] A. Molina-Sánchez, M. Palummo, A. Marini, and L. Wirtz, Temperature-dependent excitonic effects in the optical properties of single-layer MoS_2, Phys. Rev. B **93**, 155435 (2016).

[83] C. Zhang, A. Johnson, C.-L. Hsu, L.-J. Li, and C.-K. Shih, Direct imaging of band profile in single layer MoS_2 on graphite: Quasiparticle energy gap, metallic edge states, and edge band bending, Nano Lett. **14**, 2443 (2014).

[84] M.-H. Chiu, C. Zhang, H.-W. Shiu, C.-P. Chuu, C.-H. Chen, C.-Y. S. Chang, C.-H. Chen, M.-Y. Chou, C.-K. Shih, and L.-J. Li, Determination of band alignment in the single-layer Mos_2/WSe_2 heterojunction, Nat. Commun. **6**, 7666 (2015).

[85] F. Cadiz, E. Courtade, C. Robert, G. Wang, Y. Shen, H. Cai, T. Taniguchi, K. Watanabe, H. Carrere, D. Lagarde, M. Manca, T. Amand, P. Renucci, S. Tongay, X. Marie, and B. Urbaszek, Excitonic linewidth approaching the homogeneous limit in MoS_2-based van der Waals heterostructures, Phys. Rev. X **7**, 021026 (2017).

[86] H. Shin, A. K. Katiyar, A. T. Hoang, S. M. Yun, B. J. Kim, G. Lee, Y. Kim, J. Lee, H. Kim, and J.-H. Ahn, Nonconventional strain engineering for uniform biaxial tensile strain in MoS_2 thin film transistors, ACS Nano **18**, 4414 (2024).

[87] A. McCreary, R. Ghosh, M. Amani, J. Wang, K.-A. N. Duerloo, A. Sharma, K. Jarvis, E. J. Reed, A. M. Dongare, S. K. Banerjee, M. Terrones, R. R. Namburu, and M. Dubey, Effects of uniaxial and biaxial strain on few-layered terrace structures of MoS_2 grown by vapor transport, ACS Nano **10**, 3186 (2016).

[88] A. C. De Palma, G. Cossio, K. Jones, J. Quan, X. Li, and E. T. Yu, Strain-dependent luminescence and piezoelectricity in monolayer transition metal dichalcogenides, J. Vac. Sci. Technol. B **38**, 042205 (2020).

[89] D. Lloyd, X. Liu, J. W. Christopher, L. Cantley, A. Wadehra, B. L. Kim, B. B. Goldberg, A. K. Swan, and J. S. Bunch, Band gap engineering with ultralarge biaxial strains in suspended monolayer MoS_2, Nano Lett. **16**, 5836 (2016).

[90] H. Luo, X. Li, Y. Zhao, R. Yang, L. Bao, Y. Hao, Y. N. Gao, N. N. Shi, Y. Guo, G. Liu, L. Zhao, Q. Wang, Z. Zhang, G. Zhang, J. Sun, Y. Huang, H. Gao, and X. Zhou, Simultaneous generation of direct- and indirect-gap photoluminescence in multilayer MoS_2 bubbles, Phys. Rev. Mater. **4**, 074006 (2020).

[91] J. Qiao, X. Kong, Z.-X. Hu, F. Yang, and W. Ji, High-mobility transport anisotropy and linear dichroism in few-layer black phosphorus, Nat. Commun. **5**, 4475 (2014).

[92] C. E. Villegas, A. R. Rocha, and A. Marini, Anomalous temperature dependence of the band-gap in black phosphorus, Nano Lett. **16**, 5095 (2016).

[93] H. Mishra, A. Bose, A. Dhar, and S. Bhattacharya, Exciton-phonon coupling and band-gap renormalization in monolayer WSe_2, Phys. Rev. B **98**, 045143 (2018).

[94] E. Cannuccia and A. Marini, Zero point motion effect on the electronic properties of diamond, trans-polyacetylene and polyethylene, Eur. Phys. J. B **85**, 320 (2012).

[95] A. Molina-Sánchez, D. Sangalli, K. Hummer, A. Marini, and L. Wirtz, Effect of spin-orbit interaction on the optical spectra of single-layer, double-layer, and bulk MoS_2, Phys. Rev. B **88**, 045412 (2013).

[96] M. Rohlfing, P. Krüger, and J. Pollmann, Efficient scheme for GW quasiparticle band-structure calculations with applications to bulk Si and to the Si(001)-(2×1) surface, Phys. Rev. B **52**, 1905 (1995).

[97] B. Monserrat and R. J. Needs, Comparing electron-phonon coupling strength in diamond, silicon, and silicon carbide: First-principles study, Phys. Rev. B **89**, 214304 (2014).

[98] C. Attaccalite, A. Nguer, E. Cannuccia, and M. Grüning, Strong second harmonic generation in SiC, ZnO, GaN two-dimensional hexagonal crystals from first-principles many-body calculations, Phys. Chem. Chem. Phys. **17**, 9533 (2015).

[99] R. M. Chrenko, Ultraviolet and infrared spectra of cubic boron nitride, Solid State Commun. **14**, 511 (1974).

[100] G. Antonius, S. Poncé, E. Lantagne-Hurtubise, G. Auclair, X. Gonze, and M. Côté, Dynamical and anharmonic effects on the electron-phonon coupling and the zero-point renormalization of the electronic structure, Phys. Rev. B **92**, 085137 (2015).

[101] M. S. Hybertsen and S. G. Louie, Electron correlation in semiconductors and insulators: Band gaps and quasiparticle energies, Phys. Rev. B **34**, 5390 (1986).

[102] G. Antonius, S. Poncé, P. Boulanger, M. Côté, and X. Gonze, Many-body effects on the zero-point renormalization of the band structure, Phys. Rev. Lett. **112**, 215501 (2014).

[103] R. C. Chaney, E. E. Lafon, and C. C. Lin, Energy band structure of lithium fluoride crystals by the method of tight binding, Phys. Rev. B **4**, 2734 (1971).

[104] P. B. Allen and M. Cardona, Temperature dependence of the direct gap of Si and Ge, Phys. Rev. B **27**, 4760 (1983).

[105] M. Selig, G. Berghäuser, A. Raja, P. Nagler, C. Schüller, T. F. Heinz, T. Korn, A. Chernikov, E. Malic, and A. Knorr, Excitonic linewidth and coherence lifetime in monolayer transition metal dichalcogenides, Nat. Commun. **7**, 13279 (2016).

[106] G. Moody, C. K. Dass, K. Hao, C.-H. Chen, L.-J. Li, A. Singh, K. Tran, G. Clark, X. Xu, G. B. *et al.*, Intrinsic homogeneous linewidth and broadening mechanisms of excitons in monolayer transition metal dichalcogenides, Nat. Commun. **6**, 8315 (2015).

[107] P. Dey, J. Paul, Z. Wang, C. E. Stevens, C. Liu, A. H. Romero, J. Shan, D. J. Hilton, and D. Karaiskaj, Optical coherence in atomic-monolayer transition-metal dichalcogenides limited by electron-phonon interactions, Phys. Rev. Lett. **116**, 127402 (2016).

[108] Y. P. Varshni, Temperature dependence of the energy gap in semiconductors, Physica **34**, 149 (1967).

[109] J. Kopaczek, S. Zelewski, K. Yumigeta, R. Sailus, S. Tongay, and R. Kudrawiec, Temperature dependence of the indirect gap and the direct optical transitions at the high-symmetry point of the Brillouin zone and band nesting in MoS_2, $MoSe_2$, $MoTe_2$, WS_2, and WSe_2 crystals, J. Phys. Chem. C **126**, 5665 (2022).

[110] S. Bertolazzi, J. Brivio, and A. Kis, Stretching and breaking of ultrathin MoS_2, ACS Nano **5**, 9703 (2011).

[111] P. Johari and V. B. Shenoy, Tuning the electronic properties of semiconducting transition metal dichalcogenides by applying mechanical strains, ACS Nano **6**, 5449 (2012).

[112] R. G. Dickinson and L. Pauling, The crystal structure of molybdenite, J. Am. Chem. Soc. **45**, 1466 (1923).

[113] E. Cannuccia and A. Marini, *Ab initio* study of the effects induced by the electron-phonon scattering in carbon based nanostructures, arXiv:1304.0072.

[114] G. Antonius and S. G. Louie, Theory of exciton-phonon coupling, Phys. Rev. B **105**, 085111 (2022).

[115] P. B. Allen and V. Heine, Theory of the temperature dependence of electronic band structures, J. Phys. C: Solid State Phys. **9**, 2305 (1976).

[116] A. Marini, *Ab initio* finite-temperature excitons, Phys. Rev. Lett. **101**, 106405 (2008).

[117] E. Cannuccia, Giant polaronic effects in polymers: Breakdown of the quasiparticle picture, Ph.D. thesis, Rome Tor Vergata University, 2011.

[118] S. Zollner, M. Cardona, and S. Gopalan, Isotope and temperature shifts of direct and indirect band gaps in diamond-type semiconductors, Phys. Rev. B **45**, 3376 (1992).

[119] R. M. Sternheimer, Temperature dependence of the electronic structure of semiconductors and insulators, Phys. Rev. **96**, 951 (1954).

[120] S. Poncé, G. Antonius, P. Boulanger, E. Cannuccia, A. Marini, M. Côté, and X. Gonze, Verification of first-principles codes: Comparison of total energies, phonon frequencies, electron–phonon coupling and zero-point motion correction to the gap between ABINIT and QE/Yambo, Comput. Mater. Sci. **83**, 341 (2014).

[121] P. Lechifflart, F. Paleari, and C. Attaccalite, Excitons under strain: light absorption and emission in strained hexagonal boron nitride, SciPost Phys. **12**, 145 (2022).

[122] Y. Li, A. Chernikov, X. Zhang, A. Rigosi, H. M. Hill, A. M. van der Zande, D. A. Chenet, E.-M. Shih, J. Hone, and T. F. Heinz, Measurement of the optical dielectric function of monolayer transition-metal dichalcogenides: MoS_2, $MoSe_2$, WS_2, and WSe_2, Phys. Rev. B **90**, 205422 (2014).

[123] R. Saraswat, R. Verma, and S. Bhattacharya, Zenodo (2025).